Geochemistry Geophysics Geosystems G3
AN ELECTRONIC JOURNAL OF THE EARTH SCIENCES
Published by AGU and the Geochemical Society

Article
Volume 11, Number 3
23 March 2010
Q03012, doi:10.1029/2009GC002926
ISSN: 1525-2027

Click Here for Full Article

Flow rate perturbations in a black smoker hydrothermal vent in response to a mid-ocean ridge earthquake swarm

Timothy J. Crone
Lamont-Doherty Earth Observatory, Earth Institute at Columbia University, Palisades, New York 10964, USA (crone@ldeo.columbia.edu)

William S. D. Wilcock and Russell E. McDuff
School of Oceanography, University of Washington, Box 357940, Seattle, Washington 98195-7940, USA (wilcock@u.washington.edu; mcduff@ocean.washington.edu)

[1] Although there is indirect evidence for strong connections between tectonic processes and mid-ocean ridge hydrothermal flow, there are no direct observations of these links, primarily because measuring flow in these systems is difficult. Here we use an optical analysis technique to obtain a 44 day record of flow rate changes in a black smoker vent in the Main Endeavour field of the Juan de Fuca Ridge. We show that variations in the flow rate coincide with an earthquake swarm observed using an ocean bottom seismometer array. These observations indicate that connections between tectonics and flow are indeed strong, that hydraulic connections within this hydrothermal system are long ranging, and that enhanced tidal pumping of fluids may be initiated by earthquake activity. Because the effects of the swarm cross over an intervening vent field, we infer that the upflow zones feeding this field are narrow. Using the time lag between the swarm onset and the flow rate changes we estimate that the bulk permeability of the crust on the Endeavour segment ranges from 3.0×10^{-13} m^2 to 6.0×10^{-12} m^2.

Components: 7026 words, 7 figures, 1 table.

Keywords: hydrothermal; flow rates; earthquake swarms.

Index Terms: 3017 Marine Geology and Geophysics: Hydrothermal systems (0450); 7245 Seismology: Mid-ocean ridges.

Received 26 October 2009; **Revised** 26 January 2010; **Accepted** 3 February 2010; **Published** 23 March 2010.

Crone, T. J., W. S. D. Wilcock, and R. E. McDuff (2010), Flow rate perturbations in a black smoker hydrothermal vent in response to a mid-ocean ridge earthquake swarm, *Geochem. Geophys. Geosyst.*, *11*, Q03012, doi:10.1029/2009GC002926.

1. Introduction

[2] There is substantial evidence for strong connections between the flow of aqueous fluids within mid-ocean ridge hydrothermal systems and mechanical processes such as tectonic deformation and tidal loading. The most common observations suggesting such links are measurements showing fluid temperatures that vary in response to seismic activity [*Fornari et al.*, 1998; *Johnson et al.*, 2000; *Sohn et al.*, 1998] and tides [*Larson et al.*, 2007]. Chemical concentrations in vent fluids also vary with the state of tidal loading or as a result of magmatic activity [*Larson et al.*, 2007; *Lilley et al.*, 2003], and fluid pressures in off-axis boreholes can be perturbed by earthquakes [*Davis et al.*, 2001, 2004]. Observations of megaplumes occurring in

Copyright 2010 by the American Geophysical Union

response to magmatic and/or tectonic processes [*Baker et al.*, 1987; *Cann and Strens*, 1989; *Lowell and Germanovich*, 1995; *Lupton et al.*, 1999; *Wilcock*, 1997] also support the idea of such connections. Finally, numerical models suggest that tectonics and tides should have greater influence over fluid flow than over temperature or chemistry [*Crone and Wilcock*, 2005].

[3] Despite the strong but essentially indirect evidence for coupling between mid-ocean ridge hydrothermal fluid flow and mechanical processes, there have been no direct measurements of fluid flow changes in high-temperature vents in response to seismic activity. In part, the lack of such observations can be attributed to the difficulty of obtaining flow rates in seafloor hydrothermal systems. High fluid temperatures, low pH, and mineral precipitation all conspire to render invasive flow measurement techniques (such as ducted impellers [*Converse et al.*, 1984; *Schultz et al.*, 1996]) unsuitable for long term monitoring.

[4] A new technique was recently developed which allows the acquisition of relative flow rate measurements in black smoker vents using video image analysis [*Crone et al.*, 2008]. In this paper we apply this technique to time lapse video of a black smoker hydrothermal vent located in the Main Endeavour field on the Juan de Fuca Ridge to obtain a 44 day record of relative flow rate. We compare these flow data with seismic data collected during a concurrent ocean bottom seismometer study of this ridge segment [*Wilcock et al.*, 2002] and show evidence indicating that a significant earthquake swarm perturbed flow rates in the vent under video surveillance. We explore several potential implications of this observation in terms of the permeability structure of the crust and the distribution of hot fluids within the hydrothermal system.

2. Endeavour Seismic Data

[5] In the summer of 1995 a seismic network was deployed for 54 days from 10 June to 2 August on the ridge axis and west flank of the central portion of the Endeavour segment [*Wilcock et al.*, 2002] of the Juan de Fuca Ridge. The axial component of the network (Figure 1) comprised seven ocean bottom seismometers and extended along a 5 km section of the ridge axis centered on the Main Endeavour vent field. A total of 1,750 earthquakes were located with a minimum of at least 5 travel time picks including at least one S wave [*Wilcock et al.*, 2002]. Of these, 749 were located near the axis in proximity to the vent fields (defined as within 1.5 km of the center of the axial valley and within 5 km of the Main Endeavour vent field in the along axis direction). The majority of the axial earthquakes were located at 2–3 km depth and after taking into account location errors are consistent with seismicity concentrated in the hydrothermal heat uptake zone immediately above the axial magma chamber.

[6] Of the axial earthquakes, about half were assigned to seven swarms by *Wilcock et al.* [2002] each of which was relocated using cross-correlation times and the hypocentral decomposition method [*Jordan and Sverdrup*, 1981]. Two of the swarms (swarms A4 and A5 of *Wilcock et al.* [2002]) are perhaps best considered a single sequence of 179 earthquakes that lasted a little over 4 days from late on 25 June to the end of 29 June (Figures 2 and 3). The cumulative moment release for this sequence is 3×10^{13} N-m and accounts for over 60% of the total moment release for all axial earthquakes. The swarm initiated nearly 4 km north of the Main Endeavour field near the Salty Dawg field and migrated southward by about 1.5 km to a location near the High Rise field. The earthquakes define a fault plane dipping at 70° to the east beneath the west wall of the axial valley. This is orientation is consistent with earthquakes on a bounding fault of the axial valley resulting from dike induced faulting and graben subsidence [*Rubin*, 1992]. P wave first-motion focal mechanisms were obtained for seven earthquakes in the sequence but have significant uncertainties because the swarm lies near the northern limit of the network and many of the seismometers were poorly coupled.

[7] Approximating the area of fault failure by a disk [*Brune*, 1970] with an area of 2 km^2 (Figure 2) and a shear modulus of 3×10^{10} Pa, the expected slip would be between 2 mm and 0.2 m for typical stress drops ranging from 1–100 bars (10^5–10^7 Pa) [e.g., *Thatcher and Hanks*, 1983]. If the whole area of the bounding fault between the High Rise and Salty Dawg vent fields failed then either the stress drop was very small or the slip was dominantly aseismic [*Roland and McGuire*, 2009]. Alternatively, the earthquakes may be a result of propagating failure on small discrete fault patches that account for only a small portion of the fault area defined by the distribution of earthquakes. Swarms consistent with this latter explanation have been observed elsewhere [*Deichmann and Garcia-Fernandez*, 1992; *Shearer*, 1998] and may be attributed to the effects of overpressured

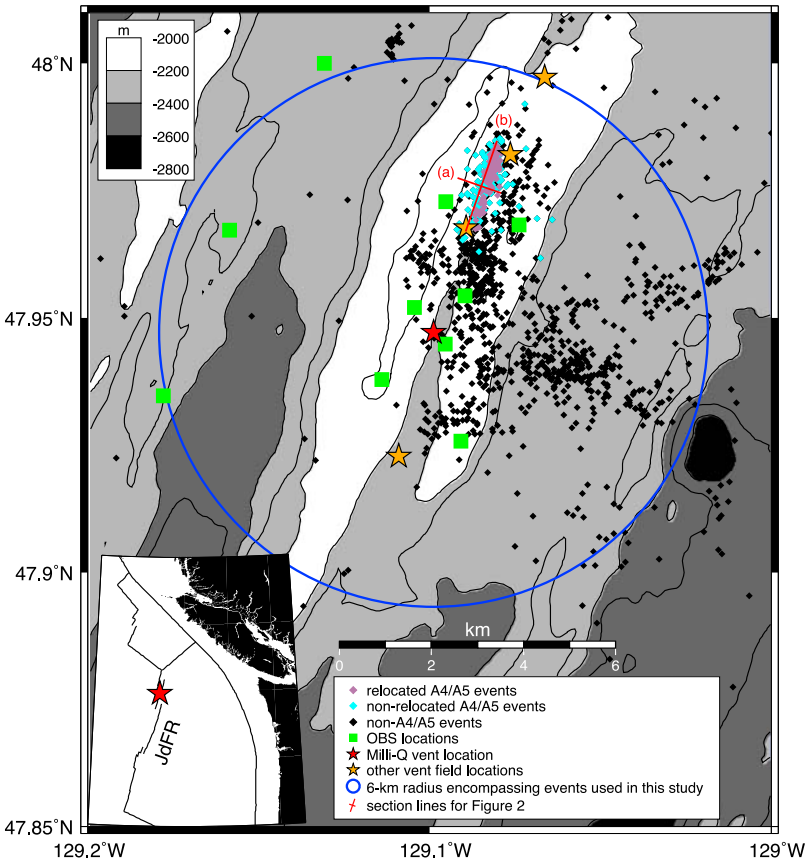

Figure 1. Bathymetric map of the Endeavour segment of the Juan de Fuca Ridge contoured at 100 m intervals showing the epicenters of earthquakes from the *Wilcock et al.* [2002] microearthquake study (diamonds). The red star shows the location of the Milli-Q vent, and the orange stars show the locations of other known vent fields on this segment. Only events within 6 km of Milli-Q are used in this study. Relocated and nonrelocated events in the A4/A5 swarm are shown with purple and blue diamonds, respectively. Section lines associated with Figures 2a and 2b are shown in red and are labeled a and b, respectively.

fluids on sealed fault patches diffusing along the fault after the patches fail [*Johnson and McEvilly*, 1995].

3. Endeavour Video Data

3.1. Field Program

[8] In the summer of 1995 a set of three Autonomous Video Camera Systems (AVCS) were deployed at three black smoker vents in the Main Endeavour field of the Juan de Fuca Ridge. The AVCS were time lapse video recorders each consisting of a pressure housing with an optically correct Lexan view port containing two Sony CCD-TR81 NTSC Hi8 camcorders and controlling electronics. One camcorder served as the camera, and the other served as a secondary recording device to give each system a 4 h recording capacity. Each system included two Deep Sea Power and Light (DSPL) Sea-Lite Maxlites with 50 watt bulbs and was powered by a 72 Ah DSPL Sea Battery.

[9] The AVCS were deployed at the Cannaport and Milli-Q vents during DSV *Alvin* dive 2937 on 16 June, and at the Grotto vent during dive 2938 on 17 June. The AVCS were recovered from Milli-Q, Cannaport, and Grotto on 16, 17, and 18 September, respectively. During the deployment the cameras were arranged so the field of view included the first ~2 m of each vent's effluent plume, and the camcorders were programmed to collect 5 s of video every hour. While the AVCS were theoretically able to collect video for 120 days with these settings, the Cannaport system lost a light just a few days into the deployment rendering the video from this vent unsuitable for flow rate analysis. The Grotto system had its autofocus mechanism enabled so it changed the focus and focal length intermittently which rendered the video from this

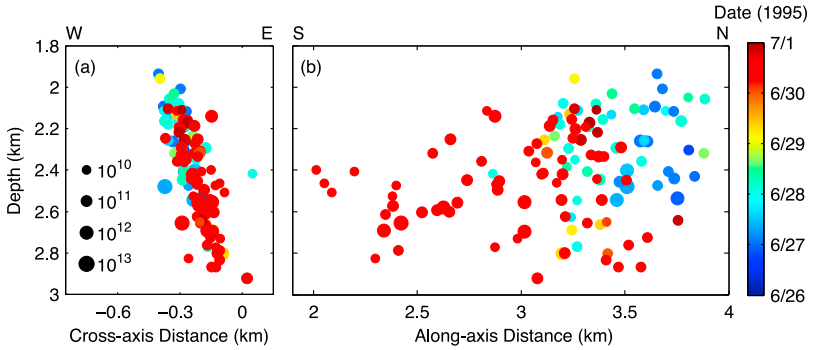

Figure 2. Cross section oriented (a) across and (b) along axis showing the projection of 122 earthquakes that were relocated using cross-correlation times by *Wilcock et al.* [2002] (Swarm A4/A5 in this paper). The earthquakes are color coded by time and scaled by seismic moment. The locations of the cross sections are shown in Figure 1.

vent unsuitable as well. The Milli-Q system's view port became clouded due to biofouling after about 44 days. In this study we analyze the first 44 days of video data from the Milli-Q vent.

3.2. Video Digitization

[10] We digitized the video image sequences from the Milli-Q vent using a Data Translation DT3152 monochrome frame grabber PCI board. We adjusted the digitizer's gain, input offset and white reference level to maximize the dynamic range of brightness in the part of the video frame with flowing fluid. Other parts of the digitized image are therefore clipped to white or black. We digitized a region of interest sized 240 × 480 pixels to include only the plume and the time stamps (Figure 4a). The digitization system was set to run continuously as the first ~90 min of the Milli-Q tape was played back on a Sony EV-S7000 which has an integrated time base corrector (TBC) which helps remove spurious sync pulses that often occur during video cassette playback.

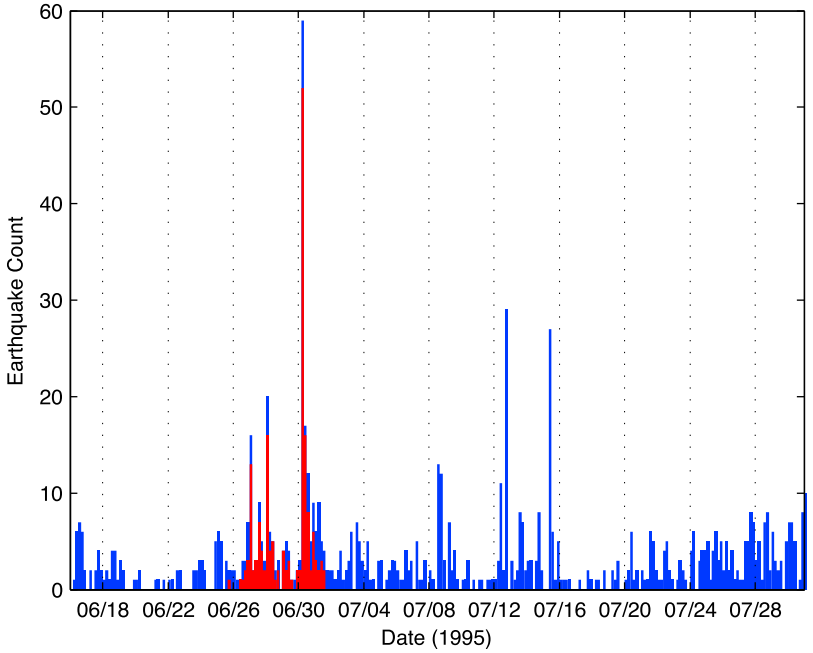

Figure 3. Histogram of all earthquakes occurring during the time period of this study that were located by *Wilcock et al.* [2002] within 6 km of the Milli-Q vent. The events that were assigned to the A4/A5 swarm are colored red. This sequence accounted for over 60% of the total moment release for all axial earthquakes observed during the 1995 study.

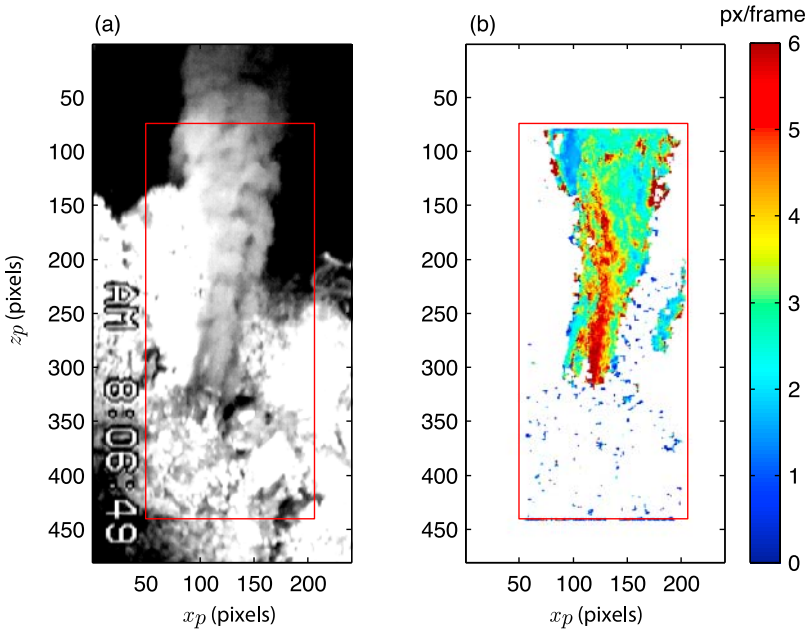

Figure 4. (a) Typical image capture from digitized video and (b) typical image velocity field computed using optical plume velocimetry (OPV). The red box shows the area of the image in which OPV was applied. Areas of the image velocity field that were masked by the roughness matrix, G, are colored white.

[11] The digitization system saved digitized video into small 1 s uncompressed AVI files with interleaved fields. We used image analysis applied to the time stamp on the video to combine and split these small files into image sequences stored as Matlab data files with the associated dates and times of collection and other metadata. Using this system we obtained 1,060 image sequences with 162–168 images in each sequence.

4. Optical Plume Velocimetry

[12] We used an image analysis technique called Optical Plume Velocimetry (OPV) to obtain a time series of the relative flow rate through the Milli-Q vent [*Crone et al.*, 2008]. The first step in this process is to compute an image velocity field for each sequence of images using temporal cross correlation. We represent each field from each image sequence as an intensity value matrix $a_{i,j,k}$, where i, j and k are index a in the z_p, x_p, and t directions, respectively. We remove the time-averaged mean from each pixel location and then calculate a cross-correlation function for a with

$$C_{i,j,l} = \sum_{k=1}^{N-l} a_{i+d,j+m,k} \cdot a_{i,j,k+l}, \qquad (1)$$

where d and m represent the separation between pixels in the z_p and x_p directions, respectively, l represents the lag number, and N is the number of frames in the sequence. To allow for flow that is not exactly aligned with the vertical, we allow the integer index m to range from −2 to 2. For the value of m that maximizes the maximal value of C, we oversample C using spline interpolation to obtain fractional lag numbers and find the interpolated lag number $l_{\max}$ corresponding to the maximal value of C. We then compute the image velocity magnitude using

$$\overline{u_p}_{i,j} = \frac{\sqrt{m^2 + d^2}}{l_{\max}}. \qquad (2)$$

We then interleave C from paired fields so the image velocity field has the same dimensions as the interleaved image sequence. Our choice of d is based on a desire to maximize $l_{\max}$ without significantly reducing the correlation coefficients in C. Larger lag numbers provide higher measurement accuracy as long as the signals correlate reasonably well. We found empirically that a pixel separation of d = 5 provided a good balance between these competing factors.

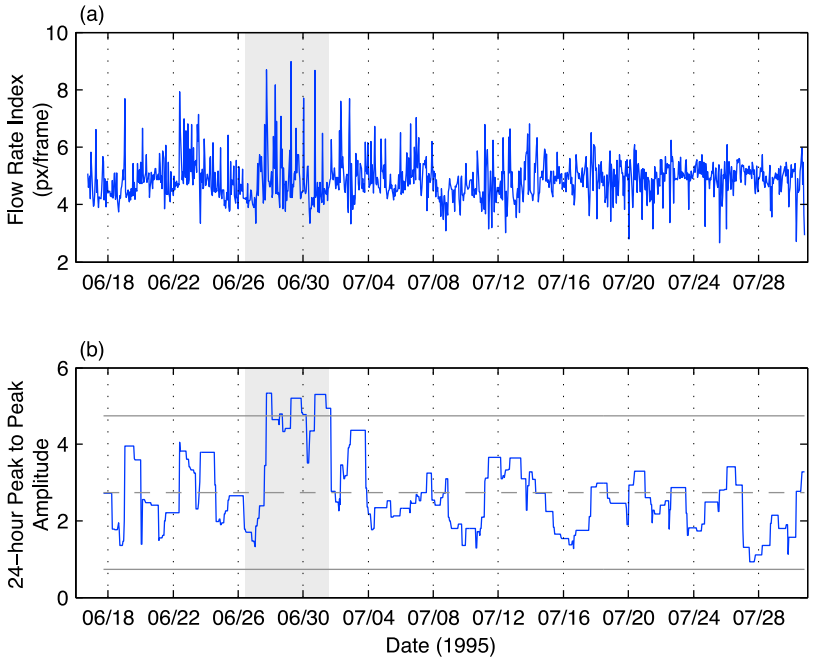

Figure 5. (a) Flow rate index computed using OPV and (b) the peak-to-peak amplitude of the flow rate index calculated using a 24 h moving window. In both plots the time period of the A4/A5 earthquake swarm is indicated with a gray shaded box. The horizontal dashed and solid gray lines show the mean and two standard deviations from the mean for the peak-to-peak values. Only during the A4/A5 swarm did the peak-to-peak values exceed two standard deviations from the mean. The time of the onset of the largest flow rate variations lags the onset of the A4/A5 swarm by 28 h.

[13] To programmatically determine the portion of the image sequence that includes flowing fluid, we compute a roughness matrix G where

$$G_{i,j} = \frac{\sqrt{\frac{1}{(2L+1)^2}\sum_{k=-L}^{L}\sum_{l=-L}^{L}\left(\overline{u_p}_{i+k,j+l} - \beta_{i,j}\right)^2}}{\beta_{i,j}}, \qquad (3)$$

and

$$\beta_{i,j} = \frac{1}{(2L+1)^2}\sum_{k=-L}^{L}\sum_{l=-L}^{L}\left(\overline{u_p}_{i+k,j+l}\right). \qquad (4)$$

G is thus the normalized standard deviation of the points in the image velocity field surrounding each image velocity value to a distance of L on all sides. Regions without flow are not well correlated in space, so they tend have a high level of roughness. This occurs in regions with fixed objects (i.e., sulfide structures) because flow rates are near zero so the normalized standard deviations amplify noise. We found empirically that when L is set to a value of 2, the region of flowing fluid can be approximately defined as the region where the roughness value is below unity.

[14] Figure 4b shows a typical image velocity field computed using this technique. The image velocity field is computed for the region of the image sequence inside the red box. Where the roughness measure is above the threshold, the image velocity values are discarded, and in Figure 4b, these areas are colored white. Finally, to compute the flow rate index for each image sequence, we discard all remaining image velocity values above 12 pixels/frame, which we deem unrealistic, and take the median of the remaining top quartile of image velocity values. We do not convert from pixels/frame to m/s because the scale of the objects in the video cannot be precisely estimated.

5. Results

[15] Figure 5 shows the 44 day flow rate index record computed from the 1,060 image sequences using OPV and the peak-to-peak amplitude of the flow rate index calculated using a 24 h moving window along with lines indicating the mean and two standard deviations from the mean for the entire record of peak-to-peak values. A shaded box

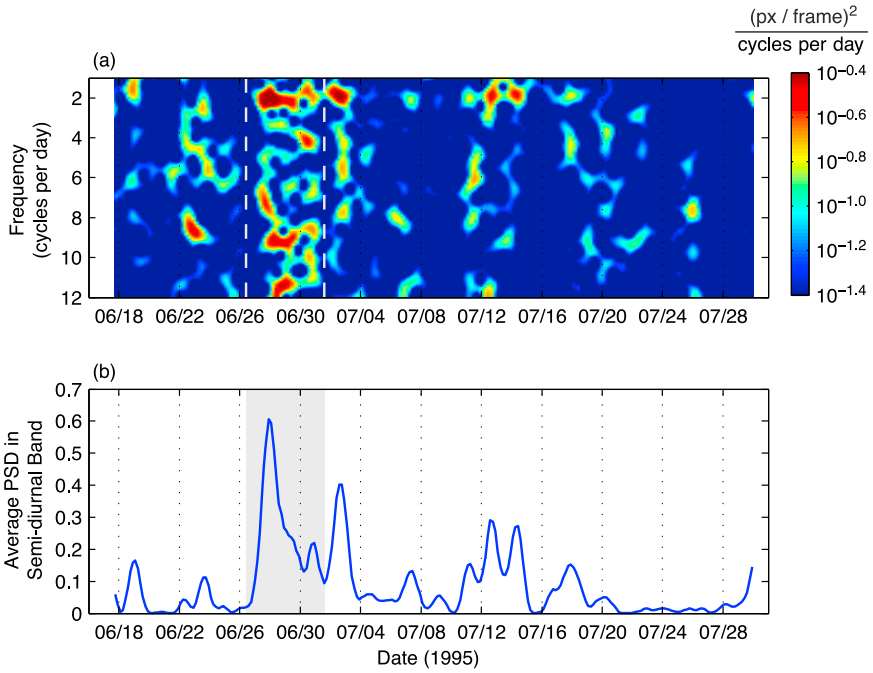

Figure 6. (a) Spectrogram showing the variation in frequency content of the flow rate index signal during the study period with the time of the A4/A5 swarm indicated with dashed lines and (b) the average power level in the frequency band 1.9–2.1 cycles per day with the time of the A4/A5 swarm shaded gray. The spectrogram was generated using 2^{10} point DFTs that were computed with 48 h Hamming windows overlapping by 44 h and then converted to one-sided power spectral density estimates.

in each panel indicates the time of the A4/A5 earthquake swarm.

[16] The long-term average flow rate did not change significantly over the measurement period, and short-term variations were typically small (<~20%), though much of the short-term variations may be related to measurement noise (see section 6.1). However, about 28 h after the start of the A4/A5 swarm the variability of the flow rate index increased significantly. This is evidenced by the large excursion of the peak-to-peak values beyond two standard deviations from the mean. Only during the A4/A5 swarm did the peak-to-peak values exceed these bounds.

[17] Figure 6 shows the spectral content of the flow rate index as it changed with time, and the signal power of this record in the frequency band surrounding the semidiurnal tidal period. About 28 h after the start of A4/A5 there was a large increase in the signal amplitude across nearly all of the measured frequency space, and this increase in energy continued until about 2 days after the nominal end of the swarm. The higher-frequency variations lagged the start of the swarm slightly more than the lower-frequency variations and appear to have diminished more quickly.

[18] Although increased variability occurred at nearly all frequencies, the variability was somewhat concentrated near a frequency of ~2 cycles per day corresponding to the semidiurnal M_2 and S_2 tidal components [*Melchior*, 1983]. The largest spike in power for the entire record occurred at ~2 cycles per day, beginning about 1 day after the start of the A4/A5 swarm and concluding about 3 days later. Another spike in this frequency band occurred just after the A4/A5 swarm, and two smaller spikes occurred about 10 days later. We did not observe any increase in power at diurnal tidal periods (e.g., K_1 or O_1).

6. Discussion

6.1. Noise

[19] The OPV technique was developed using controlled laboratory simulations of black smoker vent flows [*Crone et al.*, 2008]. One result of this research was the establishment of a set of guidelines for the collection of future seafloor video that would be optimized for OPV. The primary requirement is that the video imagery focus on the first 0.2–0.5 m of effluent, where the flow is momentum dominated and the relationship between

the average nozzle velocity and time-averaged mean free turbulent flow velocity is one-to-one linear [*Crone et al.*, 2008; *McDuff*, 1995; *Turner*, 1986]. A second requirement is high frame rate video (90–120 frames per second), which allows a reduction in d for better resolution in the fastest flowing fluid where flow structures change rapidly. A third requirement is that the video be collected with a precision machine vision digital video camera with a global shutter that halts integration on all sensor elements simultaneously. This eliminates playback noise and pixel jitter associated with the digitization of analog video, and prevents "smearing" and distortion associated with scan line data.

[20] The video analyzed in this study satisfied none of these requirements. The camera was positioned relatively far from the vent considering the focal length of the lens, so the flow of interest occupied an area of the video image that was only about 50 pixels square. The light levels were relatively low, the frame rate was the standard NTSC 30 frames per second, and the analog interleaved scan line data was noisy and slightly distorted due to smearing. For these reasons we believe that the signal to noise ratio in our flow rate data is relatively low.

6.2. Broadband Variability

[21] Despite the deficiencies of our raw data, our OPV measurements strongly suggest that the A4/A5 swarm perturbed fluid flow rates in the Milli-Q vent. While it is difficult to draw very specific conclusions from this single time series, there are a few potential implications that are worth considering. First, the distances between the earthquakes in the swarm and the Milli-Q vent are somewhat large, ranging from 2–4 km (Figure 2). There is also an intervening vent field (High Rise) between most of the swarm events and the Main Endeavour field (Figure 1). This would indicate that the hydraulic connections between different sections of the mid-ocean ridge can extend over long distances and that there are not impermeable boundaries that separate the circulation "cells" feeding different vent fields. Supporting evidence for this interpretation comes from observations of vent fluid temperature changes at Mothra (southernmost field in Figure 1) in response to a 2005 earthquake swarm occurring roughly 27 km to the north [*Hooft et al.*, 2006].

[22] Second, the passage of pressure perturbations through the hydrothermal upflow zone feeding the High Rise field may have implications for the shape and size of high-temperature upflow zones. Crust filled with very high temperature hydrothermal fluid has a high poroelastic storage capacity because the compressibility of the fluid is high [*Crone and Wilcock*, 2005]. If the High Rise upflow zone is large in its horizontal extent, it could conceivably absorb pressure perturbations generated by the swarm and diminish the effects of those pressure perturbations to the south. That this does not appear to occur suggests that high-temperature fluids in upflow zones may be constrained to relatively small volumes of crust, perhaps within pipe-like flows feeding individual vent clusters. This geometry would be consistent with the narrow alteration zones beneath vent fields inferred from crustal magnetization surveys [*Tivey and Johnson*, 2002].

[23] Finally, these results represent strong evidence that flow rates in mid-ocean ridge hydrothermal systems can be strongly influenced by mechanical forces such as tectonic activity. Flow variations that occur in response to forcings such as earthquake swarms, diking events, and tidal loading are likely very sensitive indicators of the geometry of the plumbing within mid-ocean ridge hydrothermal systems. Additional measurements of these flow variations in both high-temperature and low-temperature vents will provide strong constraints on the hydrological systems in these environments.

6.3. Tidal Variability

[24] Some of the flow rate variability appears to be concentrated in the semidiurnal tidal band (Figure 6). While it is possible that this variability is only coincidentally located in the tidal band, there are conceivable mechanisms by which the earthquake swarm could initiate tidal variability in black smoker flows.

[25] One of these mechanisms is a swarm-induced rearrangement of the permeability regime such that the hydrothermal system is "opened up" to tidal pumping. Numerical models have shown that tidal flow variations in high-temperature upflow zones may be large [*Crone and Wilcock*, 2005], and indirect measurements of flow using passive acoustic techniques have been inferred in a vent in the Main Endeavour field [*Crone et al.*, 2006]. Tidal flow variations are predicted to occur because volumes of crust filled with high- and low-temperature fluid respond differently to ocean tidal loading. However, the permeability of the crust also plays a role and changes to the permeability

structure could make the system more or less prone to this behavior. The action of the A4/A5 swarm could have introduced or removed some kind of hydraulic "shunt" or fluid pathway that made tidal perturbations possible, perhaps through a mechanism similar to one proposed by *Brodsky et al.* [2003]. This pathway may have clogged, closed mechanically, or opened back up after the conclusion of the swarm to return the system to a nontidal state.

[26] Alternatively, the A4/A5 swarm may have generated tidal perturbations directly if the earthquakes tended to be tidally triggered or if the inferred aseismic slip was influenced by tidal loading. Although the signal from tidally triggered earthquakes at mid-ocean ridges is typically small, it is a common and not insignificant feature of microearthquake catalogs from these environments [*Stroup et al.*, 2007; *Tolstoy et al.*, 2002] and such signals have been observed on this ridge segment [*Wilcock*, 2001]. Recent research has also shown that tides can generate pore pressure perturbations that propagate along axis triggering earthquakes as they go [*Stroup et al.*, 2009]. We may be observing the converse effect, whereby the earthquake swarm generated pore pressure perturbations resulting in tidal flow variations measured at the vent. There is no clear evidence from the timing of the observed earthquakes that this is indeed occurring.

[27] The signal at the semidiurnal period may simply be coincidental. The lack of a signal corresponding to diurnal tidal components (e.g., K_1 or O_1) supports this possibility, however the tidal variability may not have lasted long enough for us to resolve these low-frequency components, as we would have only observed about five cycles. *Crone et al.* [2006] observed a semidiurnal signal in vent sound production that was attributed to flow rate variations but similarly observed no diurnal signal. It is possible that some component of this system is acting like a high-pass filter. High- and low-pass filters are common in natural systems, but we have not identified any potential mechanisms for such a high-pass filter in this system. We will not likely be able to resolve this issue until we have longer time series and higher-quality data from multiple locations on the ridge axis.

6.4. Permeability Estimates

[28] Because the stiffness of seismic layer 2B is relatively high compared to the bulk modulus of fluids within the crust [*Crone and Wilcock*, 2005], we can assume that pore pressure perturbations generated by the A4/A5 swarm migrated by diffusion through the hydrothermal system, with a 28 h lag between the onset of the swarm and the flow variations. Such a situation allows us to make estimates of the bulk permeability of the crust along this section of the ridge for comparison with independent estimates made using heat flow models [*Wilcock and McNabb*, 1996; *Wilcock and Fisher*, 2004]. Caution should be used when interpreting these permeability estimates because they are calculated using flow rate measurements from a single vent, so there are considerable uncertainties associated with them.

[29] In a porous medium, the characteristic length scale, D, of pore pressure perturbations diffusing over a time, t, is given by

$$D = \sqrt{\eta t}. \tag{5}$$

The quantity η is the poroelastic hydraulic diffusivity [*Crone and Wilcock*, 2005; *Wang and Davis*, 1996],

$$\eta = \frac{k}{\mu S}, \tag{6}$$

where k is the permeability and μ is the fluid viscosity. The quantity S is the uniaxial storage compressibility,

$$S = \left(\frac{1}{K} - \frac{1}{K_s}\right)\left(1 - \frac{4\psi}{3}\right) + \phi\left(\frac{1}{K_f} - \frac{1}{K_s}\right), \tag{7}$$

where K is the drained frame bulk modulus, K_s is the solid grain (rock) bulk modulus, K_f is the fluid bulk modulus, and ϕ is the porosity of the medium. The dimensionless variable ψ is the poroelastic stress coefficient [*Detournay and Cheng*, 1993],

$$\psi = \frac{\alpha(1-2\nu)}{2(1-\nu)}, \tag{8}$$

where ν is the drained Poisson's ratio, and α is the Biot-Willis parameter,

$$\alpha = 1 - \frac{K}{K_s}. \tag{9}$$

Combining and rearranging equations (5) and (6), we obtain an equation for the permeability in terms of the length scale, D, time lag t, fluid viscosity, and the storage compressibility:

$$k = \frac{D^2 \mu S}{t}. \tag{10}$$

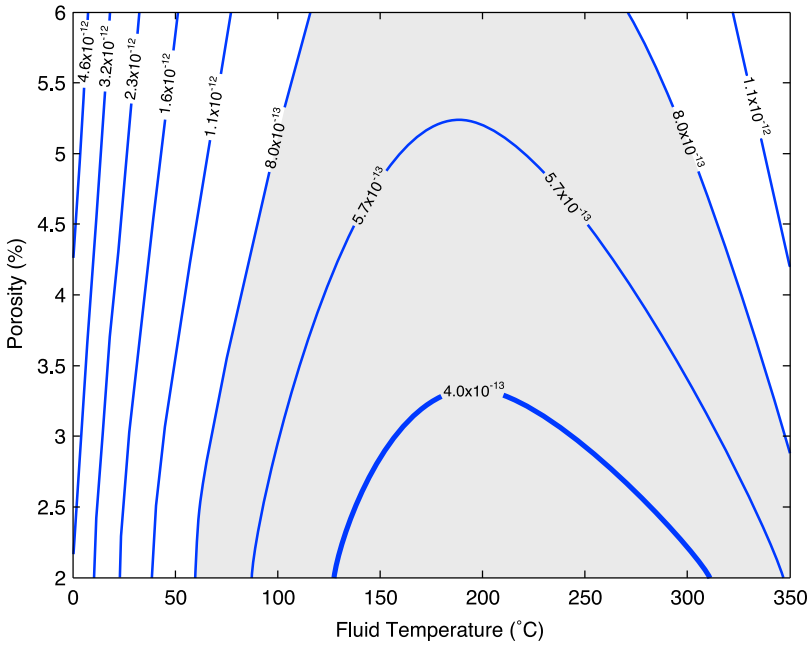

Figure 7. Contours of crustal permeability in units of m^2 estimated from the time lag of the onset of fluid flow variations and typical layer 2B/C elastic properties (Table 1) over a range of assumed fluid temperatures and crustal porosities. The bold contour (4.0×10^{-13} m^2) is the predicted value from heat flow modeling [*Wilcock and McNabb*, 1996; *Wilcock and Fisher*, 2004], and the shaded region encloses values within the formal uncertainty of the heat flow model prediction. The estimated permeability increases with an increase in the assumed porosity because the storage increases (equation (7)). The estimated permeability initially decreases with an increase in the assumed fluid temperature as the viscosity decreases but then increases at higher temperatures as the fluid bulk modulus decreases.

[30] Figure 7 shows contours of the solution to equation (10) for a range of fluid temperatures and crustal porosities assuming typical elastic properties for layer 2B/C (Table 1), a length scale of 3,500 m (Figure 2), and a time lag of 28 h. The bold contour indicates a permeability value of 4×10^{-13} m^2, the value predicted for the Main Endeavour field from the heat flow modeling [*Wilcock and McNabb*, 1996; *Wilcock and Fisher*, 2004]. The shaded area encloses permeability values within the formal uncertainty of the heat flow derived value. The estimated permeability ranges from a minimum of 3.0×10^{-13} m^2 and a maximum of x 6.0×10^{-12} m^2.

[31] If the fluids within the crust are on average relatively warm (i.e., >75°C) and have low viscosity, the time lag we observed can be explained with a crustal permeability that is similar to what is predicted by single-pass heat flow models. This possibility is supported by recent numerical modeling results showing that warm recharge fluids may be widespread and large areas of downflow may have temperatures exceeding 150°C [*Coumou et al.*, 2009; *Fontaine and Wilcock*, 2007].

[32] However if crustal fluids are cooler and more viscous, the permeability required to explain the observed time lag is a factor of ten greater. This alternative is supported by observations showing that, in general, estimates of permeability in the crust increase with increasing measurement scale [*Becker and Davis*, 2003; *Fisher*, 1998; *Renshaw*, 1998; *Sánchez-Vila et al.*, 1996]. Our permeability

Table 1. Input Parameters for Permeability Estimates

Parameter[a]	Value
K (GPa)	43.1–50.0[b]
K_s (GPa)	70[c]
K_f (GPa)	0.367–2.96[d]
ν	0.26–0.29[b]
ϕ	0.02–0.06[e]
μ (Pa s)	7.86×10^{-5}–1.80×10^{-3} [f]
t (s)	100,800
D (m)	3,500

[a]See notation section for symbol descriptions.
[b]*Crone and Wilcock* [2005].
[c]*Pros et al.* [1962].
[d]*Anderko and Pitzer* [1993] and *Pitzer et al.* [1984].
[e]*Becker* [1985].
[f]*Holzbecher* [1998].

estimates may be valid on length scales approaching 3.5 km, whereas estimates from heat flow models may only be valid on the scale of an upflow zone [*Wilcock and Fisher*, 2004].

[33] A single flow rate record from a single black smoker vent is not sufficient to resolve this issue or place significant new constraints on the permeability of the crust. However, obtaining estimates of permeability that are similar to other estimates increases our confidence that we are observing real flow rate changes. Future studies with many instruments spread across several vent fields will likely provide new insights into the permeability structure and other properties of these systems.

6.5. Future OPV Research

[34] Although the signal to noise ratio in our data set may be low because of the poor quality of the analog video, it is clear that the OPV technique has the sensitivity required to measure the flow rate variations associated with earthquake swarms. This suggests the coupling between mechanical processes and flow is strong and that flow rate variations can be large when perturbed by such forcings. This also suggests that flow rate research using optical techniques should continue. The development of modern OPV camera systems designed specifically for the task of flow measurement will have higher signal to noise ratios and will be able to more clearly delineate changes in flow and also resolve smaller changes.

[35] Multiple OPV systems deployed simultaneously at several vents across different vent fields with concurrent seismic and tidal monitoring will provide an opportunity to interpret flow rate variations with respect to their relative spatial relationships and within the context of directly measured or inferred mechanical forcings. Such a study could provide strong constraints on the permeability structure of young oceanic crust and the hydraulic connectivity between individual vents and between vent fields, as well as provide information regarding the circulation patterns of hydrothermal flow, including the nature of recharge and the depth to which flow penetrates into the lithosphere. An ambitious flow rate monitoring program has the potential to bring substantial new insights into the structure and functioning of mid-ocean ridge hydrothermal systems, their interactions with tidal, tectonic and magmatic processes, and the ways in which they support seafloor and subseafloor ecosystems.

7. Conclusions

[36] In this paper we have used an optical technique to obtain a long time series of relative flow rate through a black smoker hydrothermal vent. We have shown that the timing of variations in the flow rates during a 5 day period are nearly concurrent with an earthquake swarm occurring on a nearby bounding fault. The principal conclusions of this study are these:

[37] 1. Although the signal to noise ratio in our data may be low, the OPV technique was sufficiently sensitive to capture flow rate variations in the Milli-Q vent, and we attribute these variations to the A4/A5 swarm.

[38] 2. Hydraulic connections within the hydrothermal system are potentially long ranging and span upflow zones.

[39] 3. The presence of an intervening vent field between the swarm and the flow variations suggests that upflow zones are areas of narrowly focused high-temperature fluids.

[40] 4. The semidiurnal signal in the flow rate data may be related to tides and suggests that tidal pumping may be stopped and started by tectonic events or that tidal signals in triggering may be transmitted to flow rates in vents.

[41] 5. The permeability values inferred from the time lag between the beginning of the swarm and the initiation of flow perturbations are similar to values obtained from single-pass heat flow models, and range from 3.0×10^{-13} m^2 to 6.0×10^{-12} m^2.

[42] 6. OPV appears to be a promising technique for measuring flow rate changes in high-temperature black smoker vents. The technique should be further investigated using camera systems designed specifically for OPV, and using multiple instruments in multiple vents across vent fields.

Notation

a three-dimensional image sequence matrix.
C temporal cross-correlation function.
D characteristic pressure diffusion length scale (m).

d OPV pixel separation in the z_p direction (pixels).
G roughness matrix.
l cross-correlation lag number (frames).
l_{max} lag number at the cross-correlation maximum (frames).
L length scale for the roughness matrix (pixels).
m OPV pixel separation in the x_p direction (pixels).
N number of frames in image sequence.
t time (s).
$\overline{u_p}$ mean image velocity (pixels/frame).
x_p projected horizontal coordinate (pixels).
z_p projected vertical coordinate (pixels).
β mean of $\overline{u_p}$ to a distance of L in all directions (pixels/frame).
k permeability (m^2).
K drained frame bulk modulus (GPa).
K_f fluid bulk modulus (GPa).
K_s rock bulk modulus (GPa).
S uniaxial storage compressibility (Pa^{-1}).
t time (s).
α Biot-Willis parameter.
η hydraulic diffusivity ($m^2\ s^{-1}$).
μ fluid viscosity (Pa s).
ν drained Poisson's ratio.
ϕ porosity.
ψ poroelastic stress coefficient.

Acknowledgments

[43] We thank Brian LaFlamme, VeeAnn Atnipp Cross, and Phillip Allison for assistance with instrument development and deployment; the captain, pilots, crew, and technicians of R/V *Atlantis II* and DSV *Alvin* for assistance at sea; and Karen Bemis, Associate Editor William Seyfried Jr., and one anonymous reviewer for thorough reviews of the manuscript. Instrument development and deployment were supported by NOAA Sea Grant NA86AA-D-SG044 and NSF grant OCE-9406965, principal investigator John R. Delaney. OPV development was supported by NSF grant OCE-0623285 and by the W. M. Keck Foundation.

References

Anderko, A., and K. S. Pitzer (1993), Equation of state representation of phase equilibria and volumetric properties of the system NaCl-H_2O above 573 K, *Geochim. Cosmochim. Acta*, *57*, 1657–1680.

Baker, E. T., G. J. Massoth, and R. A. Feely (1987), Cataclysmic hydrothermal venting on the Juan de Fuca Ridge, *Nature*, *329*, 149–151.

Becker, K. (1985), Large-scale electrical resistivity and bulk porosity of the oceanic crust, Deep Sea Drilling Project Hole 504B, Costa Rica Rift, *Initial Rep. Deep Sea Drill. Proj.*, *83*, 419–427.

Becker, K., and E. E. Davis (2003), New evidence for age variation and scale effects of permeabilities of young oceanic crust from borehole thermal and pressure measurements, *Earth Planet. Sci. Lett.*, *210*, 499–508, doi:10.1016/S0012-821X(03)00160-2.

Brodsky, E. E., E. Roeloffs, D. Woodcock, I. Gall, and M. Manga (2003), A mechanism for sustained groundwater pressure changes induced by distant earthquakes, *J. Geophys. Res.*, *108*(B8), 2390, doi:10.1029/2002JB002321.

Brune, J. N. (1970), Tectonic stress and the spectra of seismic shear waves from earthquakes, *J. Geophys. Res.*, *75*, 4997–5009. (Correction, *J. Geophys. Res.*, *76*, 5002, 1971.)

Cann, J. R., and M. R. Strens (1989), Modeling periodic megaplume emission by black smoker systems, *J. Geophys. Res.*, *94*, 12,227–12,237.

Converse, D. R., H. D. Holland, and J. M. Edmond (1984), Flow rates in the axial hot springs of the East Pacific Rise (21°N): Implications for the heat budget and the formation of massive sulfide deposits, *Earth Planet. Sci. Lett.*, *69*, 159–175.

Coumou, D., T. Driesner, S. Geiger, A. Paluszny, and C. A. Heinrich (2009), High-resolution three-dimensional simulations of mid-ocean ridge hydrothermal systems, *J. Geophys. Res.*, *114*, B07104, doi:10.1029/2008JB006121.

Crone, T. J., and W. S. D. Wilcock (2005), Modeling the effects of tidal loading on mid-ocean ridge hydrothermal systems, *Geochem. Geophys. Geosyst.*, *6*, Q07001, doi:10.1029/2004GC000905.

Crone, T. J., W. S. D. Wilcock, A. H. Barclay, and J. D. Parsons (2006), The sound generated by mid-ocean ridge black smoker hydrothermal vents, *PLoS ONE*, *1*, e133, doi:10.1371/journal.pone.0000133.

Crone, T. J., R. E. McDuff, and W. S. D. Wilcock (2008), Optical plume velocimetry: A new flow measurement technique for use in seafloor hydrothermal systems, *Exp. Fluids*, *45*, 899–915, doi:10.1007/s00348-008-0508-2.

Davis, E. E., K. Wang, R. E. Thomson, K. Becker, and J. F. Cassidy (2001), An episode of seafloor spreading and associated plate deformation inferred from crustal fluid pressure transients, *J. Geophys. Res.*, *106*(B10), 21,953–21,963.

Davis, E., K. Becker, R. Dziak, J. Cassidy, K. Wang, and M. Lilley (2004), Hydrological response to a seafloor spreading episode on the Juan de Fuca Ridge, *Nature*, *430*, 335–338, doi:10.1038/nature02755.

Deichmann, N., and M. Garcia-Fernandez (1992), Rupture geomtery from high-precision relative hypocenter locations of microearthquake clusters, *Geophys. J. Int.*, *110*, 501–517.

Detournay, E., and A. H.-D. Cheng (1993), Fundamentals of poroelasticity, in *Comprehensive Rock Engineering: Principles, Practice and Projects*, vol. 2, edited by J. A. Hudson and C. Fairhurst, pp. 113–171, Pergamon, Oxford, U. K.

Fisher, A. T. (1998), Permeability within basaltic oceanic crust, *Rev. Geophys.*, *36*(2), 143–182.

Fontaine, F. J., and W. S. D. Wilcock (2007), Two-dimensional numerical models of open-top hydrothermal convection at high Rayleigh and Nusselt numbers: Implications for mid-ocean ridge hydrothermal circulation, *Geochem. Geophys. Geosyst.*, *8*, Q07010, doi:10.1029/2007GC001601.

Fornari, D. J., et al. (1998), Time-series temperature measurements at high-temperature hydrothermal vents, East Pacific Rise 9°49′–51′N, *Earth Planet. Sci. Lett.*, *160*, 419–431.

Holzbecher, E. O. (1998), *Modeling Density-Driven Flow in Porous Media*, Springer, Berlin.

Hooft, E., H. Patel, W. Wilcock, H. Berkenbosch, D. Toomey, E. Davis, D. Butterfield, R. Dziak, and M. Fowler (2006), Spatial and temporal seismicity patterns and associated vent temperature and borehole pressure perturbations of the February/March 2005 swarm on the Endeavour segment, Juan de Fuca Ridge, *Eos Trans. AGU*, *87*(52), Fall Meet. Suppl., Abstract B33D-07.

Johnson, H. P., M. Hutnak, R. P. Dziak, C. G. Fox, I. Urcuyo, J. P. Cowen, J. Nabelek, and C. Fisher (2000), Earthquake-induced changes in a hydrothermal system on the Juan de Fuca mid-ocean ridge, *Nature*, *407*, 174–177.

Johnson, P. A., and T. V. McEvilly (1995), Parkfield seismicity: Fluid driven?, *J. Geophys. Res.*, *100*, 12,937–12,950.

Jordan, T. H., and K. A. Sverdrup (1981), Teleseismic location techniques and their application to earthquake clusters in the south-central Pacfic, *Bull. Seismol. Soc. Am.*, *71*, 1105–1130.

Larson, B. I., E. J. Olson, and M. D. Lilley (2007), In-situ measurement of dissolved chloride in high temperature hydrothermal fluids, *Geochim. Cosmochim. Acta*, *71*, 2510–2523, doi:10.1016/j.gca.2007.02.013.

Lilley, M. D., D. A. Butterfield, J. E. Lupton, and E. J. Olson (2003), Magmatic events can produce rapid changes in hydrothermal vent chemistry, *Nature*, *422*, 878–881.

Lowell, R. P., and L. N. Germanovich (1995), Dike injection and the formation of megaplumes at ocean ridges, *Science*, *267*, 1804–1807.

Lupton, J. E., E. T. Baker, and G. J. Massoth (1999), Helium, heat and the generation of hydrothermal event plumes at mid-ocean ridges, *Earth Planet. Sci. Lett.*, *171*, 343–350.

McDuff, R. E. (1995), Physical dynamics of deep-sea hydrothermal plumes, in *Seafloor Hydrothermal Systems: Physical, Chemical, Biological, and Geological Interactions*, *Geophys. Monogr. Ser.*, vol. 91, edited by S. E. Humphris et al., pp. 357–368, AGU, Washington, D. C.

Melchior, P. (1983), *The Tides of the Planet Earth*, Pergamon, New York.

Pitzer, K. S., J. C. Peiper, and R. H. Busey (1984), Thermodynamic properties of aqueous sodium chloride solutions, *J. Phys. Chem. Ref. Data*, *13*, 1–106.

Pros, Z., J. Vaněk, and K. Klíma (1962), The velocity of elastic waves in diabase and greywacke under pressure up to 4 kilobars, *Stud. Geophys. Geod.*, *6*, 347–367.

Renshaw, C. E. (1998), Sample bias and the scaling of hydraulic conductivity in fractured rock, *Geophys. Res. Lett.*, *25*, 121–124.

Roland, E., and J. J. McGuire (2009), Earthquake swarms on transform faults, *Geophys. J. Int.*, *178*, 1677–1690.

Rubin, A. M. (1992), Dike-induced faulting and graben subsidence in volcanic rift zones, *J. Geophys. Res.*, *97*, 1839–1858.

Sánchez-Vila, X., J. Carrera, and J. P. Girardi (1996), Scale effects in transmissivity, *J. Hydrol.*, *183*, 1–22.

Schultz, A., P. Dickson, and H. Elderfield (1996), Temporal variations in diffuse hydrothermal flow at TAG, *Geophys. Res. Lett.*, *23*(23), 3471–3474.

Shearer, P. M. (1998), Evidence from a cluster of small earthquakes for a fault at 18 km depth beneath Oak Ridge, Southern California, *Bull. Seismol. Soc. Am.*, *88*, 1327–1337.

Sohn, R. A., D. J. Fornari, K. L. Von Damm, J. A. Hildebrand, and S. C. Webb (1998), Seismic and hydrothermal evidence for a cracking event on the East Pacific Rise crest at 9°50′N, *Nature*, *396*, 159–161.

Stroup, D. F., D. R. Bohnenstiehl, M. Tolstoy, F. Waldhauser, and R. T. Weekly (2007), Pulse of the seafloor: Tidal triggering of microearthquakes at 9°50′N East Pacific Rise, *Geophys. Res. Lett.*, *34*, L15301, doi:10.1029/2007GL030088.

Stroup, D. F., M. Tolstoy, T. J. Crone, A. Malinverno, D. R. Bohnenstiehl, and F. Waldhauser (2009), Systematic along-axis tidal triggering of microearthquakes observed at 950?N East Pacific Rise, *Geophys. Res. Lett.*, *36*, L18302, doi:10.1029/2009GL039493.

Thatcher, W., and T. C. Hanks (1983), Source parameters for Southern California earthquakes, *J. Geophys. Res.*, *78*, 8547–8576.

Tivey, M. A., and H. P. Johnson (2002), Crustal magnetization reveals subsurface structure of Juan de Fuca Ridge hydrothermal vent fields, *Geology*, *30*(11), 979–982.

Tolstoy, M., F. L. Vernon, J. A. Orcutt, and F. K. Wyatt (2002), Breathing of the seafloor: Tidal correlations of seismicity at Axial volcano, *Geology*, *30*(6), 503–506.

Turner, J. S. (1986), Turbulent entrainment: The development of the entrainment assumption, and its application to geophysical flows, *J. Fluid. Mech.*, *173*, 431–471.

Wang, K., and E. E. Davis (1996), Theory for the propagation of tidally induced pore pressure variations in layered subseafloor formations, *J. Geophys. Res.*, *101*(B5), 11,483–11,495.

Wilcock, W. S. D. (1997), A model for the formation of transient event plumes above mid-ocean ridge hydrothermal systems, *J. Geophys. Res.*, *102*, 12,109–12,121.

Wilcock, W. S. D. (2001), Tidal triggering of microearthquakes on the Juan de Fuca Ridge, *Geophys. Res. Lett.*, *28*(20), 3999–4002.

Wilcock, W. S. D., and A. T. Fisher (2004), Geophysical constraints on the sub-seafloor environment near mid-ocean ridges, in *The Subseafloor Biosphere at Mid-Ocean Ridges*, *Geophys. Monogr. Ser.*, vol. 144, edited by W. S. D. Wilcock et al., pp. 51–74, AGU, Washington, D. C.

Wilcock, W. S. D., and A. McNabb (1996), Estimates of crustal permeability on the Endeavour segment of the Juan de Fuca mid-ocean ridge, *Earth Planet. Sci. Lett.*, *138*(1–4), 83–91.

Wilcock, W. S. D., S. D. Archer, and G. M. Purdy (2002), Microearthquakes on the Endeavour segment of the Juan de Fuca Ridge, *J. Geophys. Res.*, *107*(B12), 2336, doi:10.1029/2001JB000505.